Visualization of Spokes Mode in a Hall Effect Thruster

Souradeep Roy Choudhury*, Samvram Sahu, Vara Prasad Kella, Vikash Kumar

Liquid Propulsion Systems Centre, Indian Space Research Organization,
Thiruvananthapuram, Kerala: 695547;
National Remote Sensing Centre, Indian Space Research Organization, Hyderabad, Telengana: 500084
Email: [1]souradeep28@gmail.com, [2]samvram.iist@gmail.com, [3]varapk51@gmail.com and [4]vikashkumar@lpsc.gov.in

Abstract

The present work investigates the dynamics of rotating spokes modes in a Hall Effect Thruster (HET) also known as a Stationary Plasma Thruster (SPT). Understanding these modes is important to investigate electron transport phenomena which constitute power losses for the thruster. Furthermore, the results may be inputs to future simulation studies. In this paper, post processing technique of raw images to visualize the spoke modes is presented. Images of an 85 mm mean diameter SPT anode channel, operated at 783 W at a pressure of $3.2\,x\,10^{-5}\,mbar$ *were acquired via a High-Speed Camera. The images so obtained were extremely saturated with the cathode intensity while the anode channel intensity was dominated by its DC component. Automated image processing techniques were then applied. In this process, the images were normalized with respect to the camera specifications and the cathode and anode were segmented from the anode channel image frames using Otsu's thresholding. The normalized and extracted regions are subjected to a string of post-processing involving normalization by mean image and removal of noise and the DC component. This resulted in an improved contrast as well as removal of saturation in the images due to the cathode, enabling one to focus exclusively on spokes modes.*

Keywords: *Hall Effect Thruster, Stationary Plasma Thruster, Rotating Spokes Mode*

1. Introduction

Hall Effect Thrusters find wide-range applications in space propulsion, starting from propulsion devices for orbit transfer [1] to deep space travel ([2], [3]), among others. In recent years, a significant volume of literature has been devoted to the simulation ([4, 5]) and diagnostics of HET's ([6, 7]), tackling several open problems along the way. However, the physics of the thrusters is still not fully understood. One such open problem is the anomalous cross-field electron transport.

In a typical HET, the magnetic field lines are parallel to the radial direction of the anode channel alongside an electric field along the axial direction emanating from the anode. Once placed in a magnetic field, a moving charge rotates about an axis normal to both the velocity as well as the magnetic field. For dimensions greater than the larmour radius, the charged particle makes a full rotation and hence can be confined by the magnetic field while for dimensions less than this length, the species would only be deflected away from their direction of motion.

In an HET, the anode channel depth is greater than the larmour radius of an electron but lesser than that of an ion. Hence, the electrons follow a helical path in the channel, their centers forming concentric arcs residing inside the channel where they remain confined. The ions, in contrast, are relatively unaffected by the magnetic field and free to be accelerated by the external electric field. This ideality is however, not always observed during operation of the thruster, which may give rise to several modes depending upon the operating conditions [8].

*Corresponding author: E-mail: souradeep28@gmail.com

Due to inhomogeneities in the magnetic field, interactions between electrons and the wall of the thruster channel [9], plasma instabilities [10] or other unknown factors, the electron density may fluctuate along the channel direction. The emergence of this additional fluctuating electric field along the channel leads to an axial drift velocity, referred to as the anomalous cross-field electron transport problem. This phenomenon would lead to power losses in the thruster operation, since the additional electron current would not contribute to the thrust but would consume power to sustain itself.

High speed imaging has been used as a nondestructive method to probe into these instabilities [11, 12]. The cross-field current density carried by the spokes modes has also been quantified using segmented anodes, establishing that in some cases, the spokes modes might even carry 50 % of the total current [13], leading to further insights from simulations and theoretical modeling of the phenomenon [14, 15].

While the universal cause for spokes modes is still unknown, it has been studied in a wide variety of operating conditions on a host of different thrusters [12 - 15], suggesting that spokes modes have a fundamental origin. While the physics is still not understood completely, all of the literature points to the increasing need for more experimentation, analysis, theoretical modeling as well as simulations to gather a greater variety of data under different operating conditions for different hardwares.

The current work is divided into six sections. Section 0 details the experimental setup and the various operating conditions used. Section 0 describes the various techniques applied to the images in order to extract useful information about the spokes modes. Section 0 elucidates the results of the experimentation and subsequent analysis. Section 0 ends with a few concluding remarks and possible future avenues in this direction.

2. EXPERIMENTAL SETUP AND METHODOLOGY

Experiments are carried in a cylindrical vacuum chamber with diameter 1.6 m and length 4 m. The chamber is equipped with pumping system consists of roughing pumps, turbo molecular pumps, cryo pumps and cryo cold heads. The pumping system can maintain the vacuum at $9.11 \text{ x } 10^{-5}$ mbar with Xenon load of 3 mg s^{-1}. An SPT of mean diameter 85 mm is chosen for these studies. The hardware is designed for optimized performance at 1.5 kW with 3.2 mg s^{-1} anode flow rate. However due to the facility limitations, in the present studies, the hardware was operated at a discharge voltage of 300 V, a discharge current of 2.61 A, flow rates of 30.18 mg s^{-1} and 3 mg s^{-1} for the anode and the cathode respectively. The magnets were restricted to a current of 0.7 A, with the inner magnet drawing 3.8 V while the outer magnet consumed 3.1 V. The vacuum pressure in the chamber was $3.2 \text{ x } 10^{-5}$ mbar. High speed images were acquired using Phantom make V 2012 model camera in monochrome at a rate of 60000 frames per second, with a total span of 50001 frames being captured. This led to a total time span of 0.8335 seconds. The channel was captured through the direct view port from the rear doom of the vacuum chamber. Each of the images contained 384 x 288 pixels with individual pixel intensities being 10 bit integers. Although the camera specification mentions 12 bits as the depth of each pixel, the packed raw cine files use a depth of 10 bits [15] to ensure faster transfer.

3. DATA ANALYSIS AND IMAGE PROCESSING

Reading the Images

The raw images acquired were contained in a proprietary extension, the .cine file. The file was manipulated according to the documentation [15] and the camera metadata was read, followed by the images. An open-source file reader [17] was modified to be dynamic with respect to the input files such that parameters like the image size, the frame rate and the black and whitelevels were obtained from the metadata contained in the file itself. This enabled the modified code to be able to read arbitrary image sizes, as opposed to merely 8, 16- or 48-bit pixels in the original code, proving extremely essential for the later analysis since all the pixels in the dataset were 10 bit long and could not be read by the original syntax.

Pre-processing and Post-processing

The camera uses the 'blacklevel' and the 'whitelevel' to prevent problems like oversaturation and losing out on valuable luminosity [15] by specifying the minimum and maximum intensities detectable by the sensor respectively. Hence, pixels with intensities outside this range are faulty and unreliable. Once they are discarded, the remaining valid pixels were rescaled. Both these quantities were read from the camera setup information [15], enabling further automation.

Once the images are pre-processed, the contrast for the anode channel needs to be enhanced. Following previous literature [11] as well as introducing image-processing techniques led to improvements in the image quality as well as important insights on the physics of the process.

The first step in this process was to normalize the images, as per Equation **.....**(1).

$$I_{normalized}(\boldsymbol{r},t) = \frac{\sum_{\boldsymbol{r}',t'} I(\boldsymbol{r}',t')}{\sum_{\boldsymbol{r}'} I(\boldsymbol{r}',t)} I(\boldsymbol{r},t) \quad .....(1)$$

where $I_{normalized}(\boldsymbol{r},t)$ is the intensity afternormalization at spatial position $\boldsymbol{r}$ and time t.

$I(\boldsymbol{r},t)$ is the intensity before normalization at spatial position $\boldsymbol{r}$ and time t.

As a result of this normalization, the mean of any image at a particular timestamp becomes constant, cancelling out the net temporal fluctuations. This uniformity in time enables the use of averaging methods for further image processing techniques wherein instead of each image, the mean image could be dealt with as a representative unit. Hence, the intensities were averaged over time to get an average profile $I_{mean}(\boldsymbol{r})$ for different spatial co-ordinates $\boldsymbol{r}$.

The thruster now appeared as a bright surface and the background was composed of relatively low intensities. The region could be geometrically segmented into a circular cathode, a ring-shaped anode and a background. Along the same lines, a threshold was required such that a mask could be formed by substituting all the pixels as 1 for being higher than the threshold and 0 otherwise.

Azimuthal symmetry of the anode channel allowed the use of global thresholding methods whereby the threshold is a constant independent of position. Amongst these, Otsu's thresholding algorithm [18] stands out in terms of simplicity and speed [19]. Once the pixels exceeding the threshold in intensity were singled out and the rest discarded, the nearest neighbors of all such surviving pixels were examined, both along the perpendicular axes as well as the diagonals. If the nearest neighbor of a surviving pixel also crossed the threshold, the two pixels would be part of a common blob. This was implemented using Connected Component Labeling [21], which builds on top of Union-Find strategies for Blob generation [22].

Implementing this led to the formation of two distinct blobs in the mean image corresponding to the cathode and the anode, along with a third blob in certain cases of high noise levels inside the anode cavity. Hence, in order to separate the anode, it was essential to extract the parameters of each blob, including the area of the blob in terms of number of pixels covered, its centre, edge co-ordinates and so on. The anode was then characterized by the largest area, since the cathode was isolated below it and the noisy internal channel lay entirely inside its domain.

The final image processing step would be the detection of the inner and outer radii of the anode channel. To utilize the azimuthal symmetry of the system, the mean image was transformed to polar co-ordinates around the blob centre. The maximum radius was fixed as the minimal stretch of the bounding edges containing the anode blob. The angular bins were pre-defined from 0° to 360°. The pixel intensities were interpolated from pixel co-ordinates to the required grids. For faster handling of the data, the polar intensities were averaged with respect to the angular co-ordinate to obtain an averaged intensity distribution varying with radii.

For further automation, the pixels were global thresholded once more. The outer radius r_{max}, was the distance of the farthest pixel from the centre to cross the threshold while the inner radius r_{min}, would be the distance of the farthest pixel from the centre to lie below the threshold, provided it did not exceed r_{max}. However, since the overall process was dependent on a user defined radial resolution, it was necessary to check for convergence. Hence, the ratio between r_{max} and r_{min} was computed and forced to lie within a tolerance band of the actual radius ratio of the hardware, scaled down by a factor each time the limits were violated. This ensured a self-correcting feedback as well as scaling between hardware and image.

Equipped with the radii, each image was transformed to the polar basis with the radius bounded between $[r_{min}, r_{max}]$ and the convergent radial resolution. They were then converted back to the cartesian basis again for further analysis.

Analysis

The images obtained contain information only about the anode channel where the intensities fluctuate in time as well as space. However, not all such oscillations constitute rotating spokes modes which exhibit simultaneous oscillations in time as well as space. The oscillations retaining homogeneity in time are breathing modes which eclipse the weaker spokes modes. Therefore, it is essential to remove these modes for further analysis.

Hence, the circle fit images were normalized once more followed by reduction with the mean image. This led to only oscillating components surviving, being hence called AC coupled.

To focus exclusively on the channel, the anode was cropped out with the help of the edge co-ordinates obtained during anode segmentation. This led to images with reduced area, containing just the anode channel. Apart from reducing the number of pixels, it also eliminated the need for storing the channel centre coordinates, since it now lay exactly at the centre of all images.

For visualization of only the anode channel inhomogeneities, a mask was prepared such that pixels having a radius more than the outer radius and less than the inner radius were removed. These pixels were already zero pixels deemed unnecessary for visualization. The masked images were then contour plotted together in subplots with a global colorbar.

Although the images no longer contained the cathode or other sources of noise outside the anode, they still exhibited a wide range of fluctuation across different frames. This created problems while plotting different image frames together, since setting the limits of the colorbar merely by the extrema of the intensities caused a few images to be intense whereas the rest were all at the other end of the colorbar, with no attributes to distinguish them from each other.

The colorbar limits were set at percentile values of the intensities, defined as the maximal intensity for which the cumulative probability equals the numerical value of the percentile (divided by 100). Any intensity above the maxima would then be colored the same as the colorbar maximum. This allowed the visualization of spokes modes all over the dataset.

The above process, however, was insufficient to remove the granular texture of the images. Median filtering was used wherefore each pixel, inside the bulk of the image, was placed at the centre of a rectangular window comprising of neighboring pixels. The median of this window was plotted instead of the original pixel intensity, within a bounded colorbar. This enabled clustering and removed the high degree of granularity present in the plots earlier. However, the window size, along with the percentile limits for the colorbar, had to be set based on trial and error and not automatically computed by the algorithm.

4. Results and Discussion

The parameter values are mentioned in Section 0. The rotating spokes modes seemed more probable due to the magnet currents (0.7 A) being less than the nominal value (1.3 A). For the forthcoming analysis, 20 frames were used, beginning with the first, corresponding to a time span of 0.33 seconds. The algorithm was implemented using Python 3.10 which took approximately 1 min 16.322 seconds for execution with 6 cores.

The raw data from the camera, having been pre-processed, was first visualized using contour plots with fixed and graded colorbars in grayscale, as shown in Figure 1(a). As expected, the images are highly saturated due to the cathode as well as noise, with no visible difference across frames. These images were then normalized to obtain slightly better contrast, as can be perceived from Figure 1(b).

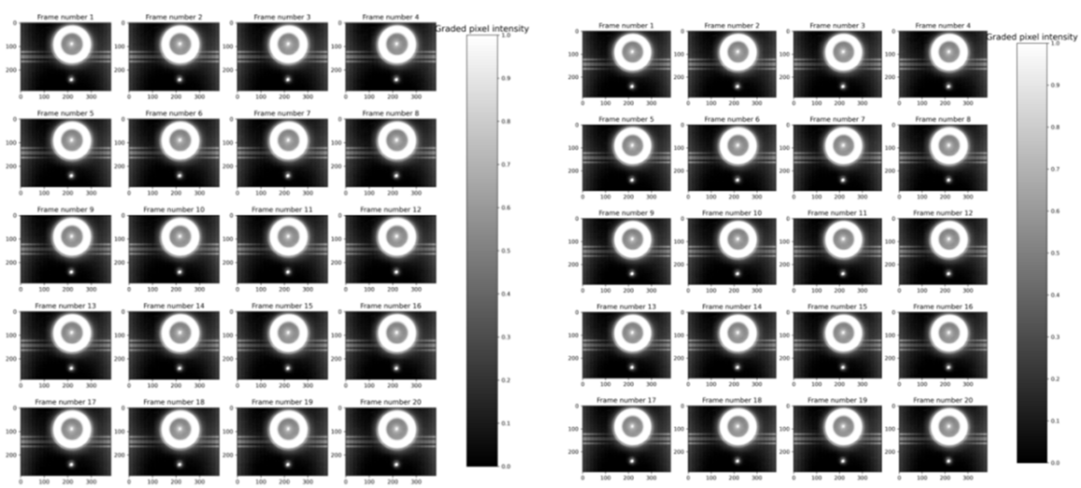

a. b.

Figure 1: (a) Camera pre-processed images, (b) Normalized images where the limits of the colorbar were kept at 10 percentile and 90 percentiles

Then the cathode was removed and the two concentric circles were fit. The initial radial resolution was 1 unit, the tolerance 0.4 and the actual radii ratio 1.5. This was processed to obtain Figure 2(a). The anode was subsequently extracted, to yield Figure 2(b).

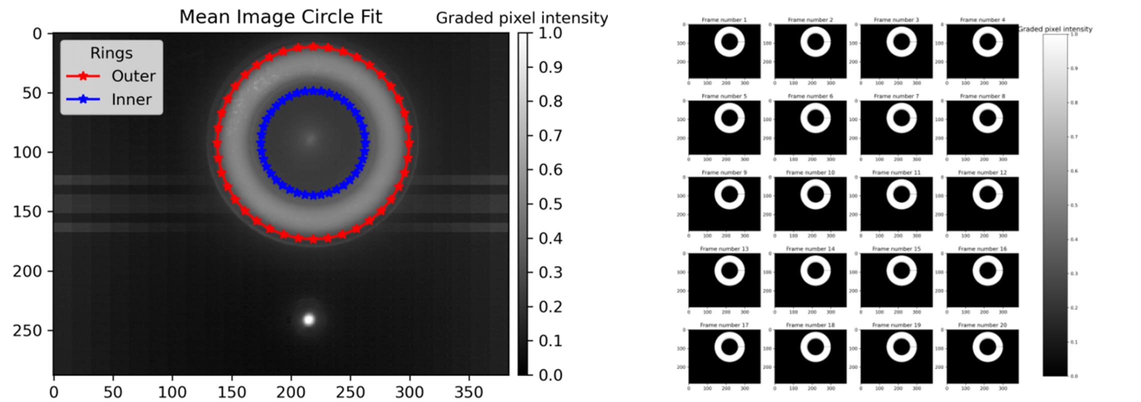

a. b.

Figure 2: (a) Fitting concentric circles on the anode channel. The colorbar was not restricted and Python default limits were not altered. (b) Cathode removal and concentric circle fitting. The colorbar limits were at 10 and 90 percentiles.

The highly saturated images were AC-coupled leading to more contrast, as shown in Figure 3(a). The colorbar was confined less than the other plots, due to the majority of pixels being zero. These cause the percentiles to be biased towards more extreme values than the usual 10 - 90 percentiles. Finally, the anode was scooped out, a mask was applied outside the channel and false color was used with a more limited colorbar due to the huge variation across the channel. The window size of five was fixed via trial and error. The final plot is shown in Figure 3(b).

The spatial inhomogeneities in the anode channel become instantly visible, with overlapping regions of high and low intensities. This set the perfect stage for visualizing the rotating spokes modes. From Figure 3(b), the spokes mode $m = 1$ is discernible, albeit not with absolute clarity. The presence of several rotating spokes modes with different temporal frequencies superimposing on each other might explain this behavior.

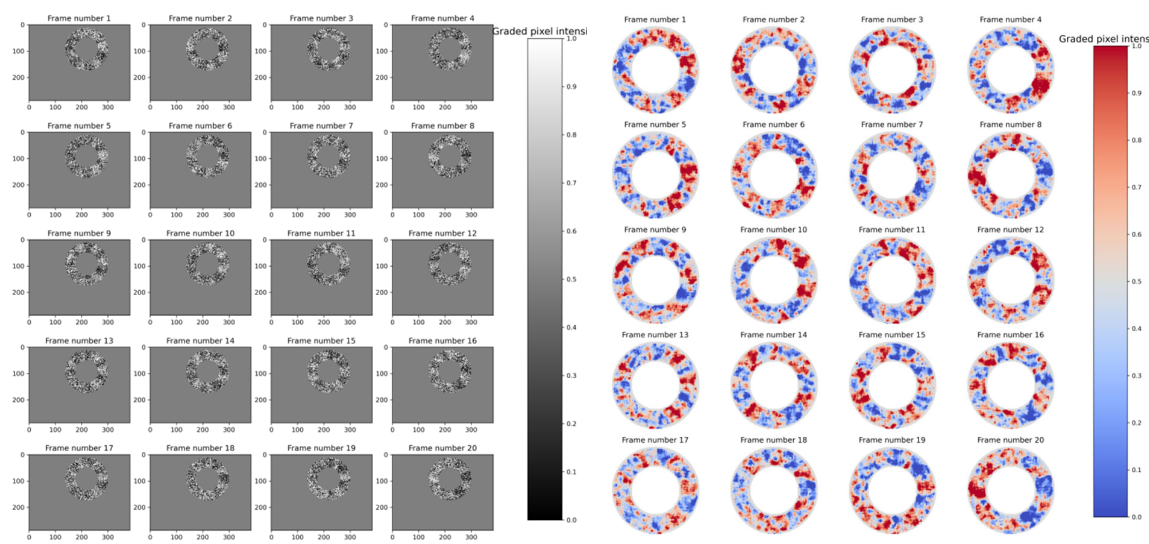

a. b.

Figure 3: (a) AC Coupled Images. The colorbar was limited between 5 and 95 percentiles. (b) Visualization of Rotating Spokes Modes. The colorbar was confined between 20 and 80 percentiles

ISBN - 978-93-95038-50-8

5. CONCLUSION

The present work describes the steps leading up to the visualization of rotating spokes modes in an HET anode channel, starting from raw images. This involved various stages of image processing, with high computational complexities. Hence, automation was a necessity, facilitated by the statistical nature of the algorithm. The plots showed a prominent $m = 1$ mode mixed with other spokes modes of varying compositions.

The next step in the analysis would be to investigate the dynamics of the images via integral transforms. This might lead to quantification of temporal as well as spatial frequencies, suitable for future simulations or experimentation.

ACKNOWLEDGEMENTS

We are grateful to Liquid Propulsions Systems Centre Valiamala, Indian Space Research Organization and National Remote Sensing Center Hyderabad, Indian Space Research Organization for supporting this work.

REFERENCES

1. Gulczinski, III, Frank, and Ronald Spores. "Analysis of Hall-effect thrusters and ion engines for orbit transfer missions." *32nd Joint Propulsion Conference and Exhibit*. 1996.
2. Koppel, Christophe R., and Denis Estublier. The SMART-1 Hall effect thruster around the moon: In flight experience. 2005, p. 119. 29th International electric propulsion conference,
3. A. Bapat, P. B. Salunkhe and A. V. Patil, "Hall-Effect Thrusters for Deep-Space Missions: A Review," in *IEEE Transactions on Plasma Science*, vol. 50, no. 2, pp. 189-202, Feb. 2022, doi: 10.1109/TPS.2022.3143032.
4. Adam, J. C., et al. "Physics, simulation and diagnostics of Hall effect thrusters." *Plasma Physics and Controlled Fusion*50.12 (2008): 124041.
5. Mikellides, Ioannis G., et al. "Hall-effect thruster simulations with 2-D electron transport and hydrodynamic ions." (2009).
6. Touzeau, M., et al. "Plasma diagnostic systems for Hall-effect plasma thrusters." *Plasma Physics and Controlled Fusion* 42.12B (2000): B323.
7. Benavides, Gabriel F., et al. "Diagnostic for verifying the thrust vector requirement of the AEPS hall-effect thruster and comparison to the NEXT-c thrust vector diagnostic." *2018 Joint Propulsion Conference*. 2018.
8. Sekerak, Michael J. *Plasma oscillations and operational modes in Hall effect thrusters*. Diss. University of Michigan, 2014.
9. Morozov, A. I., and V. V. Savel'Ev. "Theory of the near-wall conductivity." *Plasma Physics Reports* 27 (2001): 570-575.
10. Bohm, David. "The characteristics of electrical discharges in magnetic fields." *Qualitative Description of the Arc Plasma in a Magnetic Field* (1949).
11. McDonald, Michael Sean. Electron transport in Hall thrusters. University of Michigan, 2012. (Dissertation).
12. Ortega, A. Guglielmi1 A. Martıín, et al. "Influence of double-stage operation on breathing oscillations and rotating spokes in the ID-HALL thruster." (2019): 33.
13. Ellison, C. L., Y. Raitses, and Nathaniel J. Fisch. "Cross-field electron transport induced by a rotating spoke in a cylindrical Hall thruster." *Physics of Plasmas* 19.1 (2012): 013503.
14. Matyash, K., et al. "Rotating spoke instabilities in a wall-less Hall thruster: Simulations." *Plasma Sources Science and Technology* 28.4 (2019): 044002

15. Mansour, A. R., and K. Hara. "Full fluid moment modeling of rotating spokes in Penning-type configuration." *Plasma Sources Science and Technology* 31.5 (2022): 055012.
16. Vision Research. "Cine File Format" https://phantomhighspeed.my.salesforce-sites.com/servlet/fileField?id=0BE1N000000kD2i
17. Light, Adam D. (2013) "pyCine" https://github.com/adamdlight/pyCine
18. N. Otsu, "A Threshold Selection Method from Gray-Level Histograms," in IEEE Transactions on Systems, Man, and Cybernetics, vol. 9, no. 1, pp. 62-66, Jan. 1979, doi: 10.1109/TSMC.1979.4310076.
19. Perez, A. and Gonzalez, R. C. "An Iterative Thresholding Algorithm for Image Segmentation," in IEEE Transactions on Pattern Analysis and Machine Intelligence, vol. PAMI-9, no. 6, pp. 742-751, Nov. 1987, doi: 10.1109/TPAMI.1987.4767981
20. Liao, P-S., Chen, T-S. and Chung, P-C., "A fast algorithm for multilevel thresholding", Journal of Information Science and Engineering 17 (5): 713-727, 2001
21. Kensheng Wu, Ekow Otoo and Arie Shoshani, "Optimizing connected component labeling algorithms", Paper LBNL-56864, 2005, Lawrence Berkeley National Laboratory (University of California)
22. Christophe Fiorio and Jens Gustedt, "Two linear time Union-Find strategies for image processing", Theoretical Computer Science 154 (1996), pp. 165-181.